Research Article

Nano Research
2024, 17(4): 2770–2780

ISSN 1998-0124 CN 11-5974/O4
https://doi.org/10.1007/s12274-023-6201-1

Insights into the kinetics–morphology relationship of 1-, 2-, and 3D $TiNb_2O_7$ anodes for Li-ion storage

Wenlei Xu[1], Yaolin Xu[2] (✉), Veronika Grzimek[2], Andrea Martin[1], Thorsten Schultz[3,4], Patrícia A. Russo[1], Yan Lu[2], Norbert Koch[3,4], and Nicola Pinna[1] (✉)

[1] *Department of Chemistry, IRIS Adlershof and the Center for the Science of Materials Berlin, Humboldt-Universität zu Berlin, Brook-Taylor-Str. 2, 12489 Berlin, Germany*
[2] *Department of Electrochemical Energy Storage, Helmholtz-Zentrum Berlin für Materialien und Energie, Hahn-Meitner-Platz 1, 14109 Berlin, Germany*
[3] *Institut für Physik and IRIS Adlershof, Humboldt-Universität zu Berlin, Brook-Taylor-Str. 2, 12489 Berlin, Germany*
[4] *Joint Research Group of Molecular Systems, Helmholtz-Zentrum Berlin für Materialien und Energie, 12489 Berlin, Germany*

Received: 13 July 2023 / **Revised:** 12 September 2023 / **Accepted:** 14 September 2023

ABSTRACT

Understanding the influence of electrode material's morphology on electrochemical behavior is of great significance for the development of rechargeable batteries, however, such studies are often limited by the inability to precisely control the morphology of electrode materials. Herein, nanostructured titanium niobium oxides ($TiNb_2O_7$) with three different morphologies (one-dimensional (1D), two-dimensional (2D), and three-dimensional (3D)) were synthesized via a facile microwave-assisted solvothermal method. The influence of the morphological dimension of $TiNb_2O_7$ as electrode material on the electrochemical performance in Li-ion batteries (LIBs) and the underlying correlation with the electrochemical kinetics were studied in detail. 2D $TiNb_2O_7$ (TNO-2D) shows a superior rate capability and cycling stability, associated with improved kinetics for charge transfer and Li-ion diffusion, compared to the 1D and 3D materials. *Operando* X-ray diffraction measurements reveal the structural stability and crystallographic evolution of TNO-2D upon lithiation and delithiation and correlate the Li-ion diffusion kinetics with the lattice evolution during battery charge and discharge. Moreover, carbon-coated TNO-2D achieves enhanced rate capability (205 $mAh \cdot g^{-1}$ at 50 C) and long-term cycling stability (87% after 1000 cycles at 5 C). This work provides insights into the rational morphology design of electrode materials for accelerated charge transfer and enhanced fast-charging capability, pushing forward the development of electrode materials for high-power rechargeable batteries in future energy storage.

KEYWORDS

morphological dimension, electrochemical kinetics, lithium-ion batteries, $TiNb_2O_7$, structural evolution

1 Introduction

In recent years, Li-ion batteries (LIBs) have been widely used in various electric vehicles and portable devices, due to their high storage energy, long cycle lifetime, and improved safety [1–3]. To date, graphite is the dominant anode material for commercial LIBs, because of its low cost and large specific capacity (theoretically 372 $mAh \cdot g^{-1}$). Nevertheless, it is easy to form a passivating solid electrolyte interphase (SEI) at a low working potential (< 0.3 V vs Li/Li^+), causing irreversible loss of initial capacity and poor rate performance associated with sluggish Li-ion diffusion kinetics [4, 5]. Additionally, the facile formation of (Li) dendrites on the graphite surface, arising from the extremely low working potential, can grow across the separator and cause internal short circuits, leading to serious safety issues [6, 7]. As an alternative, spinel $Li_4Ti_5O_{12}$, with a high working potential of ~ 1.55 V vs Li/Li^+, enables high-rate Li (de)intercalation without the risk of SEI or Li dendrites formation. Besides, its high structural stability ensures a high cycling stability. However, its theoretical capacity (175 $mAh \cdot g^{-1}$) is low, limiting its potential for future LIBs [8–10]. Other similar Ti-based materials like $Li_5Cr_7Ti_6O_{25}$ with an enhanced theoretical capacity (320 $mAh \cdot g^{-1}$) are also considered as prospective anode materials for LIBs, but their widespread applications in LIBs are limited by their poor electronic and ionic conductivity and thus limited rate capability [11–12]. Therefore, it is still a great challenge to explore suitable anode candidates with similar merits of $Li_4Ti_5O_{12}$ but higher capacity and energy density for LIBs.

To address this issue, titanium niobium oxides with the general formula $TiNb_xO_{2+2.5x}$ (x = 2, 5, 24) have attracted considerable research interest and are regarded as promising materials to replace $Li_4Ti_5O_{12}$ anode in LIBs due to their high theoretical capacities of 387–402 $mAh \cdot g^{-1}$ (involving redox reactions between Nb^{4+}/Nb^{5+}, Nb^{3+}/Nb^{4+} and Ti^{3+}/Ti^{4+}) [13–27]. Among all of these titanium niobium oxides, $TiNb_2O_7$ is of particular interest, and has attracted widespread attention in both battery industry and academia since it was first reported as a LIB anode in 2011 [13, 15, 16, 24, 28]. $TiNb_2O_7$ has a crystallographic shear structure with 3 × 3 blocks of MO_6 (M = Ti, Nb) octahedra sharing corners and edges, which contributes to the structural stability and long-term

Address correspondence to Yaolin Xu, yaolin.xu@helmholtz-berlin.de; Nicola Pinna, nicola.pinna@hu-berlin.de

cyclability upon repetitive de-/intercalation of Li-ions [13]. Besides, the relatively high working potential (1.3–1.6 V vs Li/Li^+) of $TiNb_2O_7$ (TNO) could potentially suppress the decomposition of organic electrolyte and SEI formation [15].

In particular, nanostructured $TiNb_2O_7$ with various morphologies could deliver high rate capability and cycling stability in LIBs, benefiting from their unique structural characteristics. Note that the influence of morphological dimension of energy materials on their performance is of significant interest in the field, and there have been many studies on this topic [29, 30]. Specifically, one-dimensional (1D) patterns such as nanotubes, nanofibers, nanorods, or nanowires, show large surface-to-volume ratio, rapid electron transport along the 1D direction, short Li-ion diffusion distance along the radial direction, and restricted self-aggregation [18, 31]. Paik's group reported that hierarchical porous $TiNb_2O_7$ nanotubes display good rate capability (~ 140 $mAh{\cdot}g^{-1}$ at 50 C) [32]. Two-dimensional (2D) assemblies, such as nanosheets, exhibit large specific surface areas as well as good mechanical flexibility [27, 33]. For example, Guo's group prepared 2D nanoporous $TiNb_2O_7$ with a sol–gel method, delivering high reversible capacity and long-term cyclability (200 $mAh{\cdot}g^{-1}$ after 1000 cycles at 5 C) [34]. In comparison, three-dimensional (3D) morphologies such as nanospheres and nanoflowers normally have lower specific surface areas and slower Li-ion transport [35]. Zhu's group fabricated porous $TiNb_2O_7$ nanospheres with the assistance of block copolymer P123, demonstrating good rate performance (167 $mAh{\cdot}g^{-1}$ at 50 C) [36]. Despite the significant research progress that has been achieved, morphology–electrochemical performance relationships of $TiNb_2O_7$ as electrode materials in LIBs and the underlying mechanism remain elusive. This is because the study on the influence of morphological dimension on the electrochemical performance of $TiNb_2O_7$ has been challenged by the synthesis of a set of electrode materials with different morphological dimensions but comparable other properties (e.g., specific surface area).

In this work, we have successfully synthesized nanostructured 1D, 2D, and 3D TNO by a sol–gel synthesis and controlled their morphology by simply adjusting the concentrations of all the precursors, and measured their electrochemical performance as anode materials for LIBs. These 1D, 2D, and 3D morphology-tailored TNO materials have similar physical-chemical properties, enabling direct comparison of their electrochemical properties (including specific capacity, rate capability and cycling stability) in LIBs and hence detailed comprehension of the effects of the electrode materials morphology on their electrochemical behavior. To the best of our knowledge, this is the first time one single TNO electrode material with three different morphologies has been achieved by a template-free method to reveal the influence of morphology on the electrochemical properties in rechargeable batteries. This work reveals that 2D TNO is superior to the 1D and 3D materials as electrode materials for LIBs, especially at high current rates, which is rooted in the significantly faster kinetics of charge transfer and Li-ion diffusion in the 2D material. We have also correlated the Li-ion diffusion kinetics with the structural evolution of 2D TNO revealed by *operando* X-ray diffraction (XRD). Further enhanced rate capability (205 $mAh{\cdot}g^{-1}$ at 50 C) and cycling stability (87% capacity retention after 1000 cycles) of 2D TNO have been achieved through carbon coating, which improves the electronic conduction throughout the electrode. These findings provide insights into the role of the morphology of electrode materials in rechargeable batteries, in particular to improve the electrochemical reaction kinetics and fast charging capability.

2 Experimental section

Materials. Titanium(IV) isopropoxide (97%), cobalt(II) acetylacetonate (98%), and acetophenone (99%) were purchased from Sigma Aldrich. Niobium(V) chloride was purchased from ABCR.

Synthesis of one dimensional titanium niobium oxide (TNO-1D). TNO-1D was synthesized by dissolving titanium(IV) isopropoxide (0.167 mmol) and niobium chloride (0.333 mmol) in acetophenone (20 mL), afterward cobalt(II) acetylacetonate (0.5 mmol) was added in the solution. After being stirred for 48 h under argon, the reaction mixture was heated in a microwave reactor (Anton Paar Monowave 400) at 220 °C for 20 min, and then cooled down rapidly with compressed air. The product was collected by centrifugation, washed with acetone and ethanol thoroughly, and dried at 70 °C under air. Subsequently, the product was calcined at 700 °C for 3 h under air.

Synthesis of two and three dimensional titanium niobium oxides (TNO-2D and TNO-3D). TNO-2D was prepared by dissolving titanium(IV) isopropoxide (0.5 mmol) and niobium chloride (1 mmol) in acetophenone (20 mL), afterward cobalt(II) acetylacetonate (1 mmol) was added in the solution. For the following step, it was the same with that of TNO-1D. TNO-3D was fabricated by following the similar procedure with above, but by increasing the amount of cobalt(II) acetylacetonate from 1 to 2 mmol.

Synthesis of carbon-coated TNO-2D (TNO-2D@C). 40 mg TNO-2D was added in 20 mL 10 mM tris buffer (pH = 8.5), and the solution was sonicated for 10 min to disperse the powder. Then, 40 mg dopamine was added in the solution under stirring followed by sonication for 1 h to avoid aggregation of particles and then stirred for 2 h. The product was collected by centrifugation, washed three times with deionized water and dried at 70 °C under air. Subsequently, the product was calcined at 650 °C for 3 h under argon.

Characterization. XRD patterns were obtained using a STOE Stadi MP diffractometer equipped with Ge (111) double-crystal monochromator (Mo Kα radiation, λ = 0.70930 Å) in a transmission geometry for measurements of pristine and *ex-situ* samples and in a Bragg–Brentano geometry for *operando* measurements with a lab-designed *operando* cell [75]. One XRD pattern was recorded every hour and the *operando* cell was cycled at C/20. For comparison of the relative intensity of (020) plane, XRD measurements of TNO samples from five synthesis batches were performed to validate the reproducibility. For *ex-situ* XRD measurements of TNO samples after cycling, coin cells were disassembled, and the TNO electrodes were retrieved and rinsed several times with dimethyl carbonate (DMC) to remove the electrolyte residue. Then, the electrode film was peeled off the Cu current collector and measured as such. The Rietveld refinements were performed using the Jana2006 software [76], the shape factor (k) was 0.9. Transmission electron microscopy (TEM) and high resolution TEM (HRTEM) images were obtained on a Philips CM 200 and FEI Talos 200S microscope operated at 200 kV. Scanning electron microscopy (SEM) images were recorded with a Hitachi SU-70 HR microscope operated at 15 kV. X-ray photoelectron spectroscopy (XPS) measurements were performed in an ultrahigh vacuum setup with a base pressure of 3×10^{-10} mbar, employing the Kα-radiation of a non-monochromated Mg X-ray source (hv = 1253.6 eV) for excitation and an Omicron EA 125 hemispherical analyzer with a pass energy of 50 (20) eV for the survey (detail) scans to detect the kinetic energy of the emitted electrons. The powders were evenly distributed on carbon tape and measured without further treatment. Since charging cannot be ruled out, we refrained from interpreting the exact binding

energies. Nitrogen sorption isotherms at −196 °C were acquired on a Micromeritics ASAP 2020, after degassing the solids at 180 °C overnight.

Electrochemical measurements. Electrochemical properties of active materials (TNO-1D, TNO-2D, TNO-3D, and TNO-2D@C) were evaluated by using CR2032-type coin cells, which were assembled in an Ar-filled glovebox. First, 70% active materials, 20% conductive carbon black (Super P, Timcal), and 10% polyvinylidene fluoride (PVDF, Alfa Aesar) were homogeneously mixed with N-methyl-2-pyrrolidone (NMP, anhydrous 99.5%, Sigma-Aldrich). The resulting slurry was uniformly cast on Cu foil (Goodfellow, UK) with a doctor blade apparatus and then dried in a vacuum oven at 60 °C for 1 h. After a cold-laminating step, electrodes with a diameter of 12 mm were punched out and dried overnight at 120 °C under vacuum using a Büchi glass oven. The mass loading of active material is ≈ 1.4 mg·cm^{-2}, and the electrochemical properties using high mass loadings of 3.1 and 4.9 mg·cm^{-2} were investigated. Li metal foil was used as both counter and reference electrodes. 1 M $LiPF_6$ (ABCR, 99.9% battery grade) solution in a mixture of ethylene carbonate (EC, 99.9%, ABCR), diethyl carbonate (DEC, 99.9%, ABCR) and dimethyl carbonate (DMC, 99.9%, ABCR) with 1:1:1 volume ratio was used as the electrolyte. A glass microfiber filter (Whatman) was used as a separator. For the full cell tests, commercial $LiNi_{1/3}Co_{1/3}Mn_{1/3}O_2$ (nickel cobalt manganese (NCM), from Materials Technology International Corporation (MTI)) was used as the cathode material for LIB. The NCM cathode was prepared using a slurry including 80 wt.% NCM active material, 10 wt.% carbon black, and 10 wt.% PVDF in NMP. The mass ratio of anode to cathode was balanced based on the areal capacity ratio of anode/cathode (1:1.2) and the specific capacity of NCM cathode and TNO-2D anode. The energy density (E, Wh·kg^{-1}) and power density (P, W·kg^{-1}) of NCM||TNO-2D full cell were calculated according to the following equations

$$E = \frac{\Delta V I}{m} \quad (1)$$

$$P = \frac{E}{t} \quad (2)$$

where ΔV is the potential window (V), I is the charge/discharge current (A), m is the mass of anode and cathode active materials (g), and t is the discharge time (h).

Galvanostatic charge–discharge cycling was carried out at room temperature using a CT2001 A battery testing system (Landt Instruments). Cyclic voltammograms (CVs) were measured on a Bio-Logic VMP3 multichannel potentiostat/galvanostat with a built-in electrochemical impedance spectroscopy (EIS) analyzer. EIS was tested at open-circuit potential (OCP), in the frequency range of 100 kHz to 0.1 Hz with an amplitude of 10 mV. *In-situ* EIS analysis was performed at a current rate of 0.1 C at preselected potentials during the discharge and charge process. Galvanostatic intermittent titration technique (GITT) analysis of TNO samples was performed at a current density of 0.1 C, a current pulse of 10 min, and a rest step of 100 min.

3 Results and discussion

Figure 1 illustrates the synthesis routes of 1D, 2D, and 3D TNO (denoted as TNO-1D, TNO-2D, and TNO-3D, respectively). TNO intermediates were first prepared by a non-aqueous sol–gel method. Based on our previous study and reports from Niederberger and coworkers [37–41]. The reaction process involves aldol condensation reactions. First, niobium chloride and titanium isopropoxide react with acetophenone to produce hydroxylated niobium species and titanium-oxo clusters, titanium niobium oxide nanoparticles are then generated through condensation reactions of these monomers. TNO nanomaterials with different morphologies were formed in the presence of Co^{2+} ions. The cobalt additive acts as a promoter for the self-assembly of nanocrystals [42]. governing the morphology of TNO, and cobalt is not present in the final products, as evidenced by energy dispersive X-ray spectroscopy (EDX) and XPS (Figs. S1 and S2 in the Electronic Supplementary Material (ESM)). Then, the intermediates were annealed at 700 °C in air to improve the crystallinity.

These results suggest that Co^{2+} plays a key role in regulating the TNO morphology. Specifically, the adsorption energy and residence time of Co^{2+} on the surface of TNO crystals depend on the crystallographic facet to which Co^{2+} is adsorbing [42]. The preferential adsorption of Co^{2+} on certain facets of the TNO crystals modifies their reactivity, leading to inhibited growth rate on these facets, and thus, promoting the growth toward a specific orientation during the ripening regime [42, 43]. This proposed TNO crystal growth mechanism is similar to the previous report by Li *et al.* [44] that the presence of Al^{3+} could influence the crystal growth and eventually the morphology of Cu_3Se_2.

SEM and TEM were carried out to investigate the morphology and microstructure of the samples. SEM images (Fig. S3 in the ESM) display nanorods with lengths of 0.5–3 μm for TNO-1D, nanosheets with a thickness of ~ 50 nm for TNO-2D, and nanospheres with an average diameter of ~ 250 nm for TNO-3D. As shown in Fig. 2, all these composites are composed of nano-sized primary particles that are interconnected to form a nanoporous structure. HRTEM (Figs. 2(b), 2(f), and 2(j)) further reveals the high crystallinity of the TNO samples and the interplanar distance is measured to be 0.37 nm, corresponding to the (110) lattice plane of the monoclinic TNO. The EDX analysis of TNO-1D, TNO-2D, and TNO-3D (Fig. S1 and Table S1 in the ESM) shows Ti amounts to 33.7 at.%, 34.2 at.%, and 35.4 at.%, respectively, which are close to the stoichiometry of TNO. The selected area electron diffraction (SAED) patterns (Figs. 2(c), 2(g),

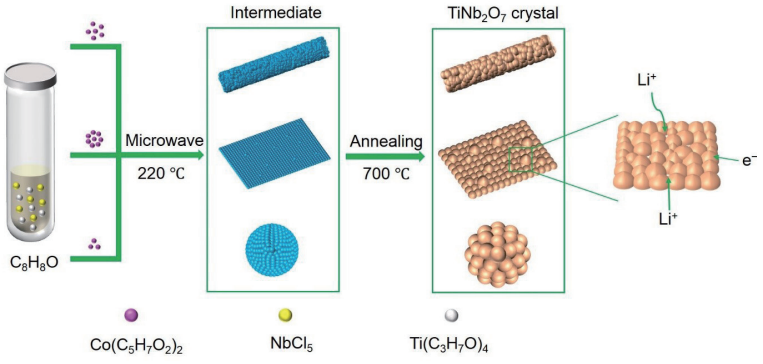

Figure 1 Schematic illustration of the synthesis route of TNO-1D, TNO-2D, and TNO-3D.

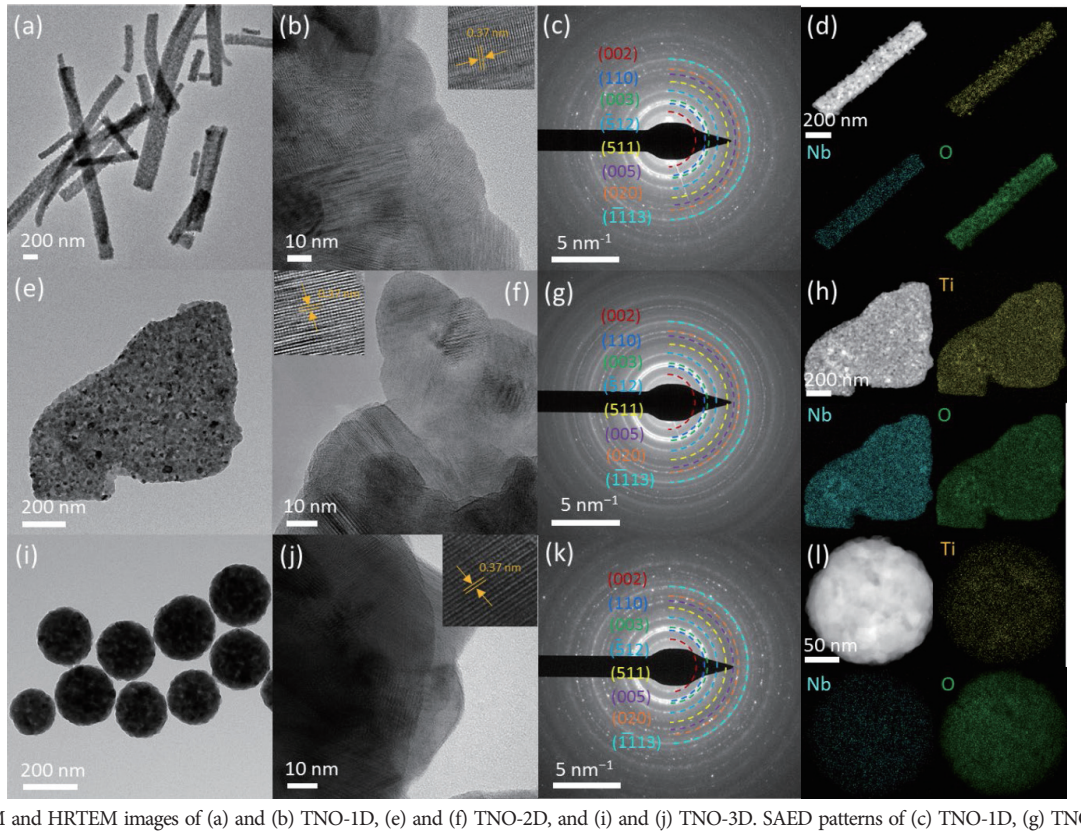

Figure 2 TEM and HRTEM images of (a) and (b) TNO-1D, (e) and (f) TNO-2D, and (i) and (j) TNO-3D. SAED patterns of (c) TNO-1D, (g) TNO-2D, and (k) TNO-3D. Scanning transmission electron microscopy combined with high angle annular dark field imagining (STEM-HAADF) and corresponding EDX elemental mappings of (d) TNO-1D, (h) TNO-2D, and (l) TNO-3D.

and 2(k)) confirm that all the samples are crystalline and match the monoclinic TNO structure. EDX elemental mappings (Figs. 2(d), 2(h), and 2(l)) display the homogeneous distribution of Ti, Nb, and O elements in the materials. SEM and TEM measurements demonstrate the successful synthesis of TNO compounds with three different morphologies.

To study the pore size distributions and specific surface areas of the composites, nitrogen adsorption–desorption experiments were performed and the results are shown in Figs. 3(a) and 3(b). TNO-2D has a Brunauer–Emmett–Teller (BET) specific surface area of 27 $m^2 \cdot g^{-1}$, which is larger than that of TNO-1D (20 $m^2 \cdot g^{-1}$) and TNO-3D (16 $m^2 \cdot g^{-1}$). The derived Barrett–Joyner–Halenda (BJH) pore size distribution curves ofTNO-1D and TNO-3D show a pore size distribution centered at ~ 20 nm, while TNO-2D has large interparticle pores. The 2D sheets reduce the tortuosity and shorten the paths of ion and electron conduction, facilitating fast and continuous charge transport and accelerating the electrochemical reaction kinetics [45, 46]. The larger pore size of TNO-2D could facilitate the infiltration of the liquid electrolyte and reduce Li-ion concentration gradient during Li-ion diffusion. These factors are important for improving the electrochemical performance, especially for the rate capability. In order to ascertain if these morphologically-tailored TNO samples have comparable other physical-chemical properties except for morphology difference, more characterizations were conducted.

The crystal structures of TNO-1D, TNO-2D, and TNO-3D have been identified by XRD measurements (Fig. 3(c)). The patterns obtained for all the three samples can be indexed to a pure-phase of $TiNb_2O_7$ (ICDD no. 00-009-0258, *C2/m* space group), demonstrating these samples possess the same crystal structures. (Note that the minor peaks at 30°–32° also originate from the diffraction of TNO (ICSD 077-1374).) The calculated crystallite sizes using the Scherrer equation are 30.9, 23.7, 25.7 nm for TNO-1D, TNO-2D, and TNO-3D, respectively. The crystal structure of TNO is built from fragments of the ReO_3-type structure in the form of blocks of corner-shared MO_6 (3 × 3, M = Ti, Nb) octahedra (Fig. 3(d)). These octahedra are assumed to be filled randomly by Ti^{4+} and Nb^{5+} ions because of their close ionic radii (Ti^{4+}: 0.61 Å, Nb^{5+}: 0.64 Å) within a six-fold oxygen coordination [47, 48]. These blocks are connected by sharing edges and bounded by crystallographic shear planes, guaranteeing a high structural stability and providing numerous vacant sites for Li-ion insertion [20, 34].

The surface chemical states of the as-synthesized samples were investigated by XPS, as shown in Fig. S4 in the ESM. The results show that the surface chemical states of Ti and Nb are similar between the three samples. The high resolution Ti 2p core level of these samples (Fig. S4(a) in the ESM) shows one characteristic doublet at 464.9 eV (Ti $2p_{1/2}$) and 459.2 eV (Ti $2p_{3/2}$) with a splitting energy of 5.7 eV, indicating that titanium is present in the 4+ oxidation state [48]. Additionally, the Nb 3d spectra (Fig. S4(b) in the ESM) exhibits two core levels at 210.2 eV (Nb $3d_{3/2}$) and 207.4 eV (Nb $3d_{5/2}$), implying that niobium is present in a 5+ valance state, as expected for $TiNb_2O_7$ [49].

Based on the above characterizations, we can conclude that TNO samples with different morphologies, but same crystal structure have been obtained successfully, enabling us to study the influence of morphology on the electrochemistry and to obtain insights into the morphology–electrochemical properties relationship of electrode materials toward improvement of battery performance. To investigate the effect of the morphology of TNO on the electrochemical properties, various electrochemical measurements were conducted to evaluate the Li-ion storage properties of the as-prepared TNO samples as electrode materials in LIBs in the potential window of 1.0–3.0 V (versus Li/Li^+). These electrode materials display similar cyclic voltammetry (CV) patterns (Figs. S5(a), S5(c), and S5(e) in the ESM), suggesting similar electrochemical response of the three TNO samples,

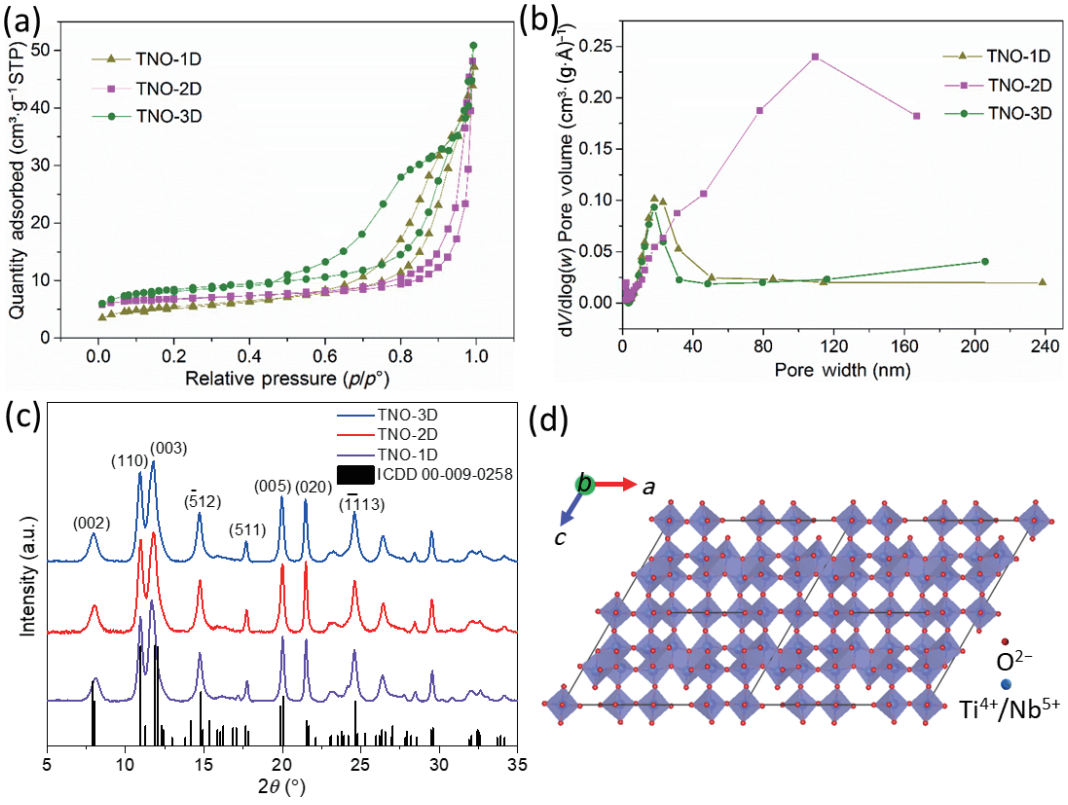

Figure 3 (a) Nitrogen adsorption–desorption isotherms and (b) corresponding pore size distribution curves of TNO-1D, TNO-2D, and TNO-3D. (c) XRD patterns of TNO-1D, TNO-2D, and TNO-3D. (d) Crystal framework of monoclinic TNO viewed along the *b*-axis.

regardless of their different morphology. Nevertheless, TNO-2D exhibits a smaller cell polarization (Fig. 4(a), and Fig. S6 and Tables S2 and S3 in the ESM) and stronger anodic/cathodic peaks, suggesting its superior electrochemical kinetics. Figure S5(c) in the ESM shows the representative CV curves of TNO-2D in the initial four cycles at a scan rate of 0.1 mV·s^{-1}. The pronounced redox peaks located at 1.71 and 1.60 V of the first cycle are ascribed to Nb^{5+}/Nb^{4+} redox couple [45]. A pair of weak and broad peaks at ~ 2.0 and 1.74 V is associated with the redox reactions of Ti^{4+}/Ti^{3+} [50, 51]. The broad bumps in the potential range of 1.0 to 1.45 V can be assigned to the Nb^{4+}/Nb^{3+} redox couple [48, 52]. After the first cycle, the CV curves almost completely overlap, indicating an outstanding reversibility and cycling stability of TNO-2D. The small shift of the peak position (1.70/1.62 V) in the following cycles could result from the electronic structure change of TNO-2D because of the irreversible lithiation in the lattice during the first cycle [17]. The average potential between the two intensive anodic/cathodic peaks at 1.70/1.62 V corresponds to the operating potential of $TiNb_2O_7$ (~ 1.66 V), similar to those of $Ti_2Nb_{14}O_{39}$ (~ 1.67 V) [53], $Cr_{0.5}Nb_{24.5}O_{62}$ (~ 1.65 V) [31], $TiNb_6O_{17}$ (~ 1.70 V) [22], and $Li_4Ti_5O_{12}$ (~ 1.57 V) [8].

Furthermore, the discharge–charge voltage profiles are also similar in shape, which is indicative of a similar electrochemical response of the TNO electrode materials (Fig. 4(b), Figs. S5(b), S5(d), and S5(f) in the ESM). The discharge/charge curve can be divided into three regions: two solid–solution regions and one two-phase coexistence region. A sloping region related to solid–solution or capacitive Li-ion storage in TNO appears at potentials larger than 1.70 V, followed by a plateau region at 1.60–1.70 V, corresponding to a two-phase transformation region. The second sloping region appears as the voltage decreases to 1.0 V in the following lithiation process. This is consistent with the previous reports on the Li-ion storage in $TiNb_2O_7$ [17–19, 24]. The discharge and charge capacities of TNO-2D in the first cycle are 290.8 and 271.5 mAh·g^{-1}, respectively, corresponding to an initial Coulomic efficiency (ICE) of 93.4%, suggesting highly reversible Li-ion intercalation and deintercalation. The high ICE of TNO-2D is critical and essential for practical application in full-cell type batteries [26]. To compensate the initial capacity loss, several strategies can be used to improve the ICE, such as creating an artificial SEI layer [54, 55], suppressing the SEI formation [56], and prelithiation [57, 58]. In the subsequent cycles, the discharge–charge curves are well overlapped, further confirming the good electrochemical reversibility and stability.

Figure 4(c) shows that TNO-2D achieves larger capacities and superior rate capability than TNO-1D and TNO-3D. When tested at 0.5, 1, 2, 5, 10, and 20 C, the TNO-2D electrode delivers reversible capacities of 272.2, 254.3, 240.1, 218.7, 203.6, 186.4 mAh·g^{-1}, respectively. At an ultrahigh current rate of 50 C (i.e., 72 s for full discharge/charge), the specific capacity is still as high as 160.2 mAh·g^{-1}, which is significantly larger than that of TNO-1D and TNO-3D at (131.9 and 104.1 mAh·g^{-1}, respectively) and close to the theoretical capacity (175 mAh·g^{-1}) of the popular $Li_4Ti_5O_{12}$. When the current rate is reset to 0.5 C, nearly 100% of the initial capacity is recovered for TNO-2D, implying its excellent reversibility. Figure 4(c) and Fig. S7 in the ESM show quantitatively the widening capacity gap between TNO-1D/3D and TNO-2D, and hence the superior rate capability of TNO-2D than TNO-1D and TNO-3D. Additionally, when these three electrodes are cycled at 5 C (Fig. 4(d)), a high capacity retention ratio of 81% is achieved for TNO-2D after 1000 cycles, which is higher than that of TNO-1D (79%) and TNO-3D (75%), supporting the superior structural stability of TNO-2D over long-term cycling. The possible reasons for the gradual capacity fading could be as follows: During long-term cycling, Li ions are repetitively inserted and extracted into/from the TNO electrode, the electrode particles suffer from mechanical stress and volume variation, and even cracks (Fig. S18 in the ESM). As a result, the SEI on the TNO surface broke and rebuilt continuously. Thus, the electrolyte decomposed continuously and Li was irreversibly

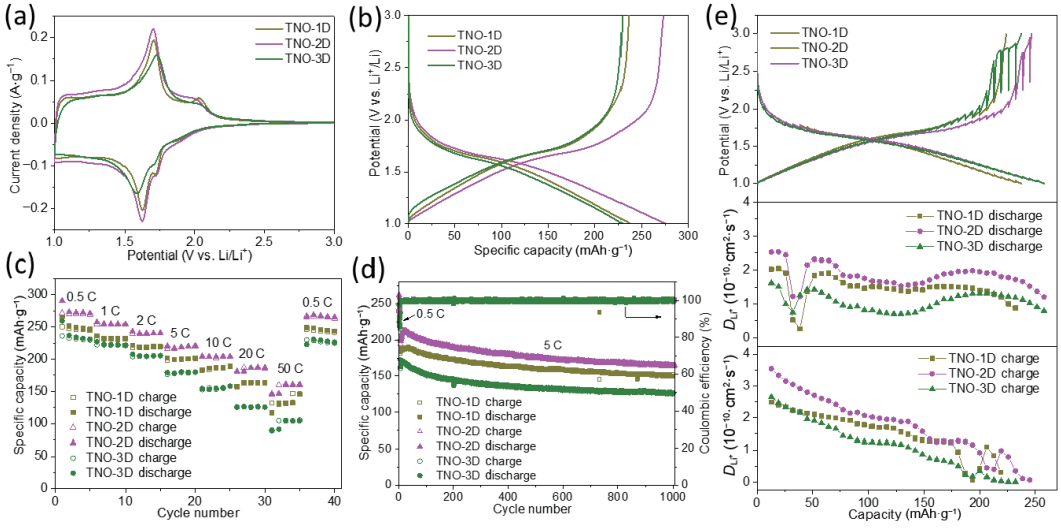

Figure 4 Electrochemical performance of 1D-, 2D-, and 3D-TNO electrodes in LIBs. (a) CV curves at 0.1 mV·s^{-1} (the 2nd cycle). (b) Galvanostatic discharge–charge curves at 0.5 C. (c) Rate capability. (d) Long-term cycling stability of the TNO samples at 5 C. (e) GITT curves and the calculated Li-ion diffusion coefficients from GITT.

consumed, leading to the gradual cell capacity loss over cycling. Besides, some other factors, such as Ohmic resistance, charge transfer resistance, generated heat due to overpotential, and possibly gas evolution caused by decomposition of electrolyte, can also lead to the gradual capacity fading. Moreover, the long-term cycling performance of TNO-2D electrode were also investigated at high current density of 50 C, as shown in Fig. S8 in the ESM. The TNO-2D electrode remains a high reversible capacity of 149.4 mAh·g^{-1} after 1000 cycles, corresponding to a retention rate of 86.2%.

The superior rate performance of TNO-2D may benefit from the faster kinetics for Li-ion uptake. Among these three TNO materials, TNO-2D exhibits the fastest kinetics of electrochemical redox reactions, as evidenced by the lowest overpotential between the cathodic–anodic peaks and the highest current response in the CV curves (Fig. 4(a)). Consistently, the differential voltage (dQ/dV) analysis reveals that TNO-2D exhibits the lowest voltage hysteresis between discharge and charge, indicative of its facilitated kinetics of Li-ion storage (Fig. S6 in the ESM). To understand in-depth the superior electrochemical redox kinetics of TNO-2D, we have performed galvanostatic intermittent titration technique (GITT), *in-situ* EIS, and CV at various scan rates.

The GITT results reveal the Li-ion diffusivity in the TNO solids. Figure 4(e) shows typical GITT curves of TNO samples. The Li-ion diffusion coefficient can be estimated by using Fick's second law through the following equation [59, 60]

$$D_0 = \frac{4}{\pi\tau}\left(\frac{m_B V_M}{M_B S}\right)^2\left(\frac{\Delta E_S}{\Delta E_\tau}\right)^2\left(\tau \ll \frac{L^2}{D_0}\right) \quad (3)$$

where D_0 is the ionic diffusion coefficient (cm^2·s^{-1}), V_M is the molar volume of the active material, M_B is the molecular mass of the active material, m_B is the mass of the active material in the electrode, L is the electrode thickness, S is the surface area of the electrode (1.13 cm^2), τ is the duration of a current pulse, ΔE_S is the change in the equilibrium potential, and ΔE_τ is the change in potential after the pulse. The last two parameters can be obtained from the voltage profiles during the GITT test (Fig. S9 in the ESM).

As shown in Fig. 4(e), the Li-ion diffusion coefficients of TNO-2D varies between 1.2 × 10^{-10} and 2.5 × 10^{-10} cm^2·s^{-1} during lithiation and decreases from 3.5 × 10^{-10} to 7 × 10^{-12} cm^2·s^{-1} during delithiation. They are markedly higher than those of TNO-1D and TNO-3D, indicating that TNO-2D possesses faster Li-ion diffusion kinetics which enable a superior rate capability. D_0 remained relatively stable at the initial stage of lithiation before a sharp decrease occurred at ~ 1.75 V. The drastic dip could be rooted in the onset of the two-phase transformation reaction of TNO during lithiation, which has a higher energy barrier for Li-ion diffusion [20, 61]. D_0 resumed at the potential of ~ 1.70 V as the phase transformation proceeds, and then decreased slowly until the capacity reached 150 mAh·g^{-1} (i.e. $Li_{1.94}TiNb_2O_7$), which could be attributed to the increased columbic repulsion between the inserted Li-ions. After that, the D_0 values increased slightly and then decreased gradually again. The increase in D_0 can be explained as a result of further exothermal reaction effects caused by the Nb^{4+}/Nb^{3+} redox reaction, which accelerates Li-ion migration [24, 50]. While the decrease in D_0 could be ascribed to the full occupancy of the active storage sites as the phase became overlithiated and to the distortion of the local structure [62, 63]. During the delithiation process, D_0 dropped gradually as Li-ions were extracted, due to the low electronic conductivity and thus large resistance of the delithiated phase [17]. A dramatic drop was observed at ~ 1.85 V, which could be related to the termination of the two phase transformation and structural reorganization. When the voltage is below ~ 1.60 V, the Li-ion diffusion coefficient of TNO compounds is higher during the Li-ion extraction than that in the Li-ion insertion process, revealing that lithiation is a less kinetically favorable process as compared to delithiation and hence the rate-limiting step for the discharge–charge cycling of TNO-based LIBs. In contrast, when the voltage is above ~ 1.60 V, the kinetics of Li-ion extraction becomes the limiting factor for fast-charging [20].

In-situ and *ex-situ* EIS measurements provide insights into the kinetics of charge transfer and Li-ion diffusion. As displayed in Fig. S10 in the ESM, the Nyquist plot is generally composed of a depressed semicircle in the high-to-medium frequency region and a slope in the low frequency range. The proposed equivalent circuit is included in the figure. The high-frequency intercept at the x-axis is the bulk resistance (R_1) of the electrolyte, separator, and electrode. The depressed semicircle at high-medium frequencies represents charge transfer resistance (R_2) at the electrode/electrolyte interface. CPE_1 and C_{int} are constant phase element and pseudocapacitance, respectively. The inclined line in the low frequency region is related to the Warburg resistance (Z_W), which reflects the solid-state diffusion of Li-ion in the bulk electrode [64, 65]. The fitted resistance values are listed in Table S4

in the ESM. It is noteworthy that TNO-2D presents the smallest charge transfer resistance and hence fastest electrochemical kinetics, benefiting from the 2D assembled TNO network. This result is consistent with the CV measurements and differential voltage analyses. It is apparent that the charge transfer resistance decreased significantly after cycling, indicating the enhanced electrochemical reaction kinetics and accelerated charge transfer of TNO electrode during lithiation/de-lithiation process (Fig. S11 in the ESM). Figure S12 in the ESM shows the Nyquist and Bode plots of the *in-situ* EIS results of TNO samples at various lithiation and delithiation states. The frequencies at the end of the charge-transfer-related semicircles are listed in Table S5 in the ESM. The higher the frequency, the faster the charge transfer. Interestingly, all the three samples show the same frequency varying trend during discharge and charge. The frequencies at 1.60–1.75 V during both discharge and charge processes are much lower than that at other potentials, indicating much slower charge transfer and hence sluggish reaction kinetics during the two-phase transformantion [27, 66]. In comparison, the frequencies gradually increase when the voltage reduces from 1.60 to 1.0 V, indicative of accelerated charge transfer, which is related to the solid–solution and/or capacitive Li-ion storage at the voltage slope, probably due to the accumulation of Li-ions in the crystal structure leading to increased coulombic repulsion of the inserted Li-ions [17, 34]. Meanwhile, the phase angles decrease with the decrease of potential from 1.6 to 1.0 V, which also supports the fast charge transfer and dominance of capacitive storage during this voltage range [67].

CV measurements of TNO electrodes under various sweep rates unveil quantitative contributions from capacitive (surface-controlled) and Faradaic (diffusion-controlled) Li-ion storage processes. The relationship between the current (i) and the sweep rates (v) follows the power law [49, 68, 69]

$$i = av^b \tag{4}$$

where a and b are adjustable values and the b parameter can be obtained from the slope of the log(i) versus log(v) plot. In particular, a b-value of 0.5 means a diffusion-controlled process, while a b-value of 1 indicates a capacitive process. Figure S13 in the ESM shows the CV curves with varied sweep rates and the plots of log(i) versus log(v) for both the cathodic and anodic peaks of TNO samples. The b values are found to be between 0.70 and 0.90, which indicates the achieved capacities are contributed by both Li-ion insertion in TNO and capacitive charge storage. Besides, the b values of TNO-2D are relatively larger than those of TNO-1D and TNO-3D, revealing that TNO-2D has a higher capacitive contribution, due to its larger specific surface area and pore size facilitating faster kinetics of Li-ion insertion/extraction.

The current response (i) at a fixed potential can be utilized to quantitatively determine the contributions of capacitive (k_1v) and diffusion-controlled ($k_2v^{0.5}$) processes according to [77]

$$i = k_1v + k_2v^{0.5} \tag{5}$$

where v is the sweep rate, constants (k_1 and k_2) can be calculated from the plots of $i/v^{0.5}$ versus $v^{0.5}$ followed by linear regression. The quantitative results (Fig. S14 in the ESM) suggested that all the samples exhibit significant capacitive behavior. This could be ascribed to the typical Wadsley–Roth shear structure [16], which provides a tunnel structure for pseudocapacitive behavior accompanied by a Faradaic charge storage process [26, 70]. The high capacitive behavior is related to the lower resistance for charge transfer as well as Li-ion diffusion [66], which has been demonstrated by EIS and GITT analyses. In addition, the larger capacitive Li-ion storage also contributes to the superior rate capability of TNO-2D.

The rapid Li-ion and electron transport of TNO-2D enables a high capacity retention even at a high areal mass loading. As shown in Fig. S15 in the ESM, TNO-2D electrodes with three mass loadings (1.5, 3.1, and 4.9 mg·cm^{-2}) were studied. It can be seen that the mass loading can significantly alter the galvanostatic charge–discharge characteristics (Figs. S15(a) and S15(b) in the ESM). The charge–discharge curves of the TNO-2D electrodes show an increasing voltage drop and capacity loss with the increase of mass loading. This indicates that TNO-2D electrode shows an increasingly larger internal resistance with increasing mass loading, which results in higher overpotentials and lower capacity [71]. This highlights the challenges in delivering sufficient charges (such as Li ions) to keep the same specific capacity in thicker electrodes. However, at a high rate of 10 C, capacities of 164 and 129 mAh·g^{-1} can still be maintained with 3.1 and 4.9 mg·cm^{-2} mass loadings, respectively (Fig. S15(c) in the ESM). Moreover, after 300 cycles at 5 C, the TNO-2D electrodes with mass loadings of 3.1 and 4.9 mg·cm^{-2} retain capacities of 176 and 148 mAh·g^{-1}, corresponding to capacity retention rates of 87.6% and 78.7% (Fig. S15(d) in the ESM), respectively. These results suggest the excellent rate performance and cycling stability of TNO-2D, even at an elevated mass loading.

To understand the underlying correlation between the favorable electrochemical redox kinetics of TNO-2D and its morphological characteristics, we have carried out *operando* XRD to elucidate the evolution of the crystal structure of TNO-2D during de-/lithiation (Fig. 5 and Fig. S16 in the ESM). Note that, compared to coin cells, the *operando* XRD cell exhibited larger overpotentials during dis-/charge and achieved lower capacities, which was caused by its low stacking pressure. Before cycling, all the diffraction peaks can be indexed to $TiNb_2O_7$, except for the ones associated with the Bragg diffraction of Fe and Be, which are from the *operando* cell setup. It is noticed that all reflections shift to lower angles during lithiation, because of the expansion of $TiNb_2O_7$ lattice induced by the Li-ions insertion. The shifts are almost fully recovered to their original Bragg peak positions and intensities upon extraction of Li-ions. Additionally, no newly peaks emerged or disappeared during the repeated Li-ions insertion–extraction processes, demonstrating the high structural stability and electrochemical reversibility of TNO-

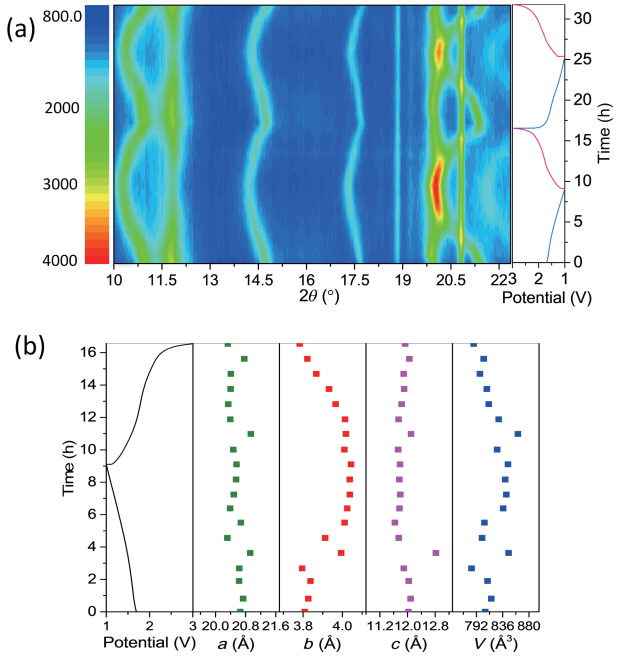

Figure 5 (a) Contour plot of the *operando* XRD pattern for TNO-2D at C/20 for the first two cycles with the discharge and charge curves. (b) Lattice parameter evolution of TNO-2D.

2D during cycling and Li-ions occupied some particular sites rather than substituted the component of $TiNb_2O_7$ during lithiation [31]. $TiNb_2O_7$ can be classified as a typical intercalation-type anode material with a robust shear ReO_3 crystal structure [72]. Its lithiation–delithiation mechanism can be described by Eq. (6)

$$TiNb_2O_7 + xe^- + xLi^+ \leftrightarrow Li_xTiNb_2O_7 (0 \le x \le 5) \quad (6)$$

In addition, the lattice parameter values (*a*, *b*, *c*, and unit cell volume (*V*)) resulting from the Rietveld refinement of *operando* diffraction data are plotted in Fig. 5(b). As can be seen, the *a* and *c* are relatively stable, while the *b* and *V* variations are obviously larger, reaching increases of 6.2% and 4.7% after discharging to 1.0 V, respectively. The changes of the lattice parameters are almost completely reversed during the subsequent delithiation process, further supporting the high reversibility of the redox reactions. The fact that the unit-cell volume variation was mainly caused by the increase of the *b*-value indicates that the Li-ion diffusion could be facilitated along the (020) plane, which is consistent with previous reports [20, 34, 72]. The increased *b* value can be ascribed to the increased columbic repulsion among the inserted Li ions, which are accumulated in the (020) plane upon Li-ion insertion. As shown in Table S6 in the ESM, TNO-2D shows higher relative intensity of the (020) plane, implying that TNO-2D has more favorable channels for Li-ion diffusion, which further supports the superior electrochemical performance of TNO-2D. Based on these results, (020) faceted single crystal TNO would exhibit significantly enhanced Li-ion diffusion. However, its experimental validation still requires great advance in the synthesis of single crystal with controlled morphology. Meanwhile, the drastic changes of lattice parameters at around 1.55 V could be caused by the lattice distortion and structure rearrangement to tolerate Li-ions insertion during the phase transition reaction process [17, 27]. Such variations can induce significant lattice stress/strain and result in inhomogeneous reactions [34, 61], which requires more energy for the insertion and extraction of Li-ions inside the $TiNb_2O_7$ crystal lattice, and thus leads to sluggish kinetics, as discussed above.

In addition, *ex-situ* XRD measurements were carried out to investigate the phase changes of TNO-1D, TNO-2D, and TNO-3D after long-term cycling (Fig. S17 in the ESM). It is apparent that the diffraction peaks remain unchanged after 1000 cycles. Meanwhile, the morphologies can be retained after long-term cycling (Figs. S18(a)–S18(c) in the ESM), but cracks can be observed, especially in TNO-3D (Figs. S18(d)–S18(f) in the ESM). It is worth noting that, though the insertion of Li-ions along the (020) plane may induce increased lattice strain, the low thickness (~ 50 nm), i.e., large surface/thickness ratio, of the TNO-2D can alleviate effectively the lattice strain, which has been evidenced by the structural stability of TNO-2D upon repetitive Li-ion de-/intercalation. As shown in Figs. S17 and S18 in the ESM, the TNO-2D electrode retained its original crystal structures and morphologies after 1000 cycles, suggesting that the strain-induced crystal structure degradation of TNO on Li-ion de-/intercalation is insignificant.

These findings highlight the role of the morphology, of electrode materials in the electrochemical performance. The superior electrochemical performance of TNO-2D benefits from the following merits of the 2D morphology (Fig. 6(a)). (i) The 2D nanostructure exhibits a larger specific surface area and interparticle porosity, which features provide a larger contact area between electrolyte and active materials and shortens Li^+ diffusion length. It not only provides more accessible sites for Li-ion storage, but also facilitates fast Li-ion diffusion, leading to improved electrochemical kinetics for Li-ion uptake. (ii) The micron-sized 2D assembly of nanoparticles endows continuous pathways for in-plane ion transport and a nanometer distance for through-plane ionic diffusion (Fig. 6(b)). (iii) TNO-2D has increased ratio of the (020) lattice plane, along which the Li-ion diffusion is favored (Fig. 6(c)). (iv) 2D morphology is stable against volume variation, alleviating the mechanical stress generated during cycling [17, 34]. The factors (i)–(iii) synergistically facilitates fast kinetics of charge transfer and Li-ion transport, resulting in significant enhancement

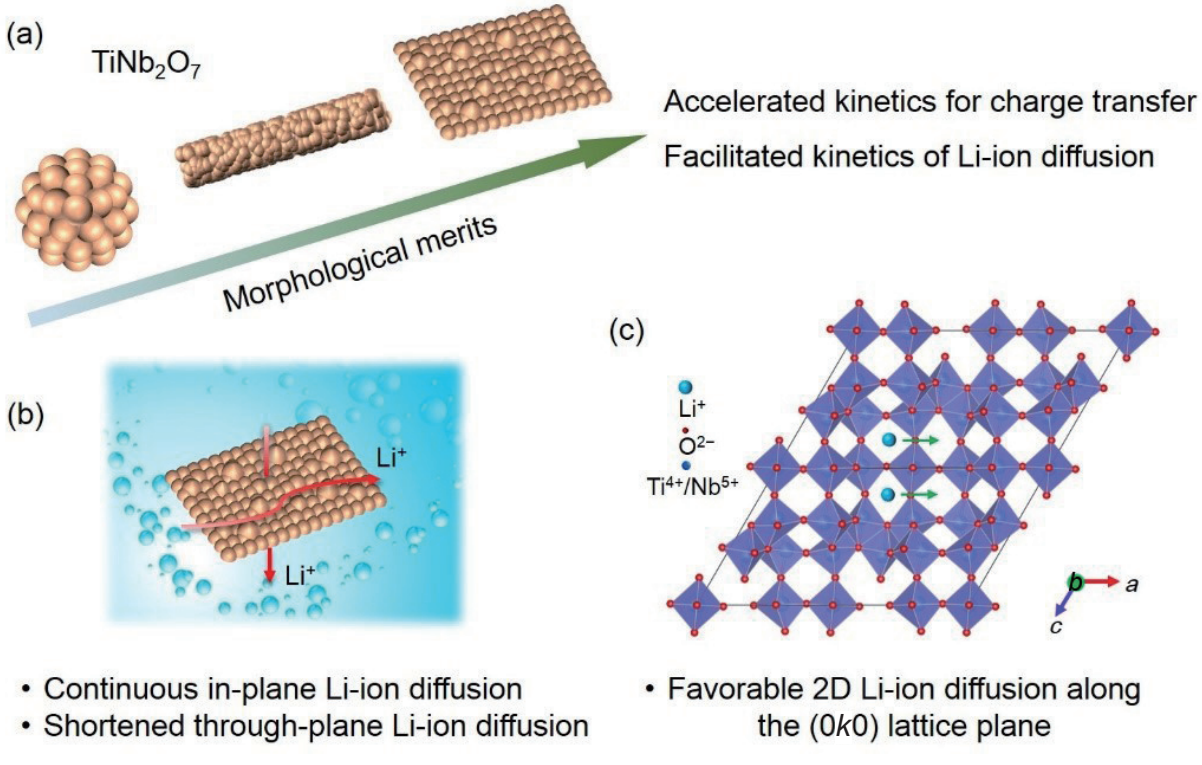

Figure 6 (a) Morphological merits of TNO. (b) Schematic illustration of the lithiation process in TNO-2D. (c) Li-ion diffusion along *ac* plane of TNO crystal structure.

of the rate capability of TNO-2D as electrode materials in LIBs [73, 74]; while merit (iv) leads to enhanced structural integrity over cycling and hence excellent cycling stability.

To further improve the electrochemical performance of TNO-2D, carbon coating was used for TNO-2D, denoted by TNO-2D@C. As shown in Figs. S19 and S20 in the ESM, it has similar physical-chemical properties as TNO-2D. By comparing its electrochemical properties with those of TNO-2D (Fig. S21 in the ESM), the rate performance, especially at high rates, was significantly improved (205 $mAh{\cdot}g^{-1}$ at 50 C) as well as cycling stability (87% capacity retention after 1000 cycles), demonstrating its promise for application in LIBs. The improvement of electrochemical performance of TNO-2D@C could be attributed to the improved electronic conductivity of electrode materials and reduced charge transfer resistance (Fig. S22 in the ESM) benefiting from the carbon coating. Besides, the carbon coating can suppress the volume changes during de-/lithiation and stabilize the SEI layer [24].

In the end, a $LiNi_{1/3}Co_{1/3}Mn_{1/3}O_2$ (NCM)||TNO-2D full cell was tested to evaluate the potential of TNO-2D for practical applications (Fig. S23 in the ESM). The electrochemical properties was investigated in the potential range of 1.5–3.0 V, the areal capacity ratio of anode compared to cathode was 1:1.2. The full cell delivers high specific capacities of 268.1, 248.2, 227.6, 205.0, and 162.9 $mAh{\cdot}g^{-1}$ at 0.2, 0.5, 1, 2, and 5 C, respectively (Figs. S23(a) and S23(b) in the ESM). After 300 cycles at 5 C, a high reversible capacity of 131.7 $mAh{\cdot}g^{-1}$ is retained with a capacity retention rate of ~ 80% (Fig. S23(c) in the ESM), indicating a good cycling stability. Moreover, the full cell exhibits a maximum gravimetric energy density of 236.9 $Wh{\cdot}kg^{-1}$ at 0.2 C with a power density of 68.3 $W{\cdot}kg^{-1}$. When cycling at 5 C, the power output reaches 1743.3 $W{\cdot}kg^{-1}$, while the gravimetric energy density amounts to 146.4 $Wh{\cdot}kg^{-1}$ (Fig. S23(d) in the ESM).

4 Conclusion

In this work, we have successfully synthesized 1D, 2D, and 3D TNO with a simple sol–gel synthesis method, and measured their electrochemical performance as electrode material for LIBs to investigate the influence of the morphology on the electrochemical properties and the underlying mechanism. It reveals that the rate capability and cycling stability of TNO-2D is superior to TNO-1D and TNO-3D, which is found to be rooted in its enhanced kinetics for charge transfer and about one order of magnitude faster kinetics of Li-ion diffusion in TNO during de-/lithiation, benefiting from the morphological merits of the 2D assembly of TNO nanoparticles. *Operando* XRD allowed us to further correlate the faster Li-ion diffusion kinetics with the favorable Li-ion diffusion along the (020) lattice plane, and also revealed the high reversibility of the structural evolution of TNO-2D during de-/lithiation that is associated with the excellent cycling stability. Moreover, carbon-coating of TNO-2D further improved its fast charge capability (205 $mAh{\cdot}g^{-1}$ at 50 C) and cycling stability (capacity retention of 87% at 5 C after 1000 cycles), contributed by the enhanced electronic conductivity and hence accelerated charge transfer kinetics and improved structural stability, respectively.

In conclusion, this work has unveiled relationship between the morphology of TNO and its electrochemical performance as electrode material in LIBs, and correlated it with the kinetics of charge transfer and Li-ion diffusion. It highlights the importance of tailoring the morphology of electrode materials for improving the performance of LIBs. Our TNO materials could serve as a model electrode material for LIBs and beyond, and the findings obtained in this work provide insights toward the rational design and engineering of electrode materials for future rechargeable batteries, in particular to improve fast charging capability. Nevertheless, the kinetics–morphological dimension relationship achieved in this work is likely to be only valid for intercalation-type electrode materials, which exhibit limited volume changes upon de-/lithiation. Conversion- and alloy-type electrode materials that exhibit large volume expansion/shrinkage upon lithiation/delithiation suffer from severe pulverization along cycling, thus the influence of the initial morphology would be limited.

Acknowledgements

Wenlei Xu acknowledges the fellowship from the China Scholarship Council (CSC). Christoph Erdmann and Xuefeng Pan are acknowledged for TEM and SEM measurements, respectively. Yu Wang and Wei Zhang are acknowledged for fruitful discussions.

Electronic Supplementary Material: Supplementary material (Figs. S1–S23 and Tables S1–S6) is available in the online version of this article at https://doi.org/10.1007/s12274-023-6201-1.

Funding note: Open Access funding enabled and organized by Projekt DEAL.

References

[1] Li, M.; Lu, J.; Chen, Z. W.; Amine, K. 30 years of lithium-ion batteries. *Adv. Mater.* **2018**, *30*, 1800561

[2] Lukatskaya, M. R.; Dunn, B.; Gogotsi, Y. Multidimensional materials and device architectures for future hybrid energy storage. *Nat. Commun.* **2016**, *7*, 12647.

[3] Noori, A.; El-Kady, M. F.; Rahmanifar, M. S.; Kaner, R. B.; Mousavi, M. F. Towards establishing standard performance metrics for batteries, supercapacitors and beyond. *Chem. Soc. Rev.* **2019**, *48*, 1272–1341.

[4] Downie, L. E.; Krause, L. J.; Burns, J. C.; Jensen, L. D.; Chevrier, V. L.; Dahn, J. R. *In situ* detection of lithium plating on graphite electrodes by electrochemical calorimetry. *J. Electrochem. Soc.* **2013**, *160*, A588–A594.

[5] Goodenough, J. B.; Kim, Y. Challenges for rechargeable Li batteries. *Chem. Mater.* **2010**, *22*, 587–603.

[6] von Sacken, U.; Nodwell, E.; Sundher, A.; Dahn, J. R. Comparative thermal stability of carbon intercalation anodes and lithium metal anodes for rechargeable lithium batteries. *J. Power Sources* **1995**, *54*, 240–245.

[7] Zheng, G. Y.; Lee, S. W.; Liang, Z.; Lee, H. W.; Yan, K.; Yao, H. B.; Wang, H. T.; Li, W. Y.; Chu, S.; Cui, Y. Interconnected hollow carbon nanospheres for stable lithium metal anodes. *Nat. Nanotech.* **2014**, *9*, 618–623.

[8] Zhao, B. T.; Ran, R.; Liu, M. L.; Shao, Z. P. A comprehensive

review of $Li_4Ti_5O_{12}$-based electrodes for lithium-ion batteries: The latest advancements and future perspectives. *Mater. Sci. Eng. R: Rep.* **2015**, *98*, 1–71.

[9] Yuan, T.; Tan, Z. P.; Ma, C. R.; Yang, J. H.; Ma, Z. F.; Zheng, S. Y. Challenges of spinel $Li_4Ti_5O_{12}$ for lithium-ion battery industrial applications. *Adv. Energy Mater.* **2017**, *7*, 1601625.

[10] Yi, T. F.; Xie, Y.; Zhu, Y. R.; Zhu, R. S.; Shen, H. Structural and thermodynamic stability of $Li_4Ti_5O_{12}$ anode material for lithium-ion battery. *J. Power Sources* **2013**, *222*, 448–454.

[11] Wei, T. T.; Peng, P. P.; Ji, Y. R.; Zhu, Y. R.; Yi, T. F.; Xie, Y. Rational construction and decoration of $Li_5Cr_7Ti_6O_{25}$@C nanofibers as stable lithium storage materials. *J. Energy Chem.* **2022**, *71*, 400–410.

[12] Yi, T. F.; Mei, J.; Peng, P. P.; Luo, S. H. Facile synthesis of polypyrrole-modified $Li_5Cr_7Ti_6O_{25}$ with improved rate performance as negative electrode material for Li-ion batteries. *Compos. Part B: Eng.* **2019**, *167*, 566–572.

[13] Hu, L.; Luo, L. J.; Tang, L. F.; Lin, C. F.; Li, R. J.; Chen, Y. J. $Ti_2Nb_{2x}O_{4+5x}$ anode materials for lithium-ion batteries: A comprehensive review. *J. Mater. Chem. A* **2018**, *6*, 9799–9815.

[14] Deng, Q. L.; Fu, Y. P.; Zhu, C. B.; Yu, Y. Niobium-based oxides toward advanced electrochemical energy storage: Recent advances and challenges. *Small* **2019**, *15*, 1804884.

[15] Han, J. T.; Huang, Y. H.; Goodenough, J. B. New anode framework for rechargeable lithium batteries. *Chem. Mater.* **2011**, *23*, 2027–2029.

[16] Han, J. T.; Goodenough, J. B. 3-V full cell performance of anode framework $TiNb_2O_7$/Spinel $LiNi_{0.5}Mn_{1.5}O_4$. *Chem. Mater.* **2011**, *23*, 3404–3407

[17] Lu, X.; Jian, Z. L.; Fang, Z.; Gu, L.; Hu, Y. S.; Chen, W.; Wang, Z. X.; Chen, L. Q. Atomic-scale investigation on lithium storage mechanism in $TiNb_2O_7$. *Energy Environ. Sci.* **2011**, *4*, 2638–2644.

[18] Tang, K.; Mu, X. K.; van Aken, P. A.; Yu, Y.; Maier, J. "Nano-Pearl-String" $TiNb_2O_7$ as anodes for rechargeable lithium batteries. *Adv. Energy Mater.* **2013**, *3*, 49–53

[19] Park, H.; Wu, H. B.; Song, T.; Lou, X. W.; Paik, U. Porosity-controlled $TiNb_2O_7$ microspheres with partial nitridation as a practical negative electrode for high-power lithium-ion batteries. *Adv. Energy Mater.* **2015**, *5*, 1401945.

[20] Griffith, K. J.; Seymour, I. D.; Hope, M. A.; Butala, M. M.; Lamontagne, L. K.; Preefer, M. B.; Koçer, C. P.; Henkelman, G.; Morris, A. J.; Cliffe, M. J. et al. Ionic and electronic conduction in $TiNb_2O_7$. *J. Am. Chem. Soc.* **2019**, *141*, 16706–16725.

[21] Lyu, H.; Li, J. L.; Wang, T.; Thapaliya, B. P.; Men, S.; Jafta, C. J.; Tao, R. M.; Sun, X. G.; Dai, S. Carbon coated porous titanium niobium oxides as anode materials of lithium-ion batteries for extreme fast charge applications. *ACS Appl. Energy Mater.* **2020**, *3*, 5657–5665.

[22] Lin, C. F.; Wang, G. Z.; Lin, S. W.; Li, J. B.; Lu, L. $TiNb_6O_{17}$: A new electrode material for lithium-ion batteries. *Chem. Commun.* **2015**, *51*, 8970–8973.

[23] Li, S. H.; Chen, J. W.; Gong, X. F.; Wang, J. X.; Lee, P. S. Holey graphene-wrapped porous $TiNb_{24}O_{62}$ microparticles as high-performance intercalation pseudocapacitive anode materials for lithium-ion capacitors. *NPG Asia Mater.* **2018**, *10*, 406–416.

[24] Takami, N.; Ise, K.; Harada, Y.; Iwasaki, T.; Kishi, T.; Hoshina, K. High-energy, fast-charging, long-life lithium-ion batteries using $TiNb_2O_7$ anodes for automotive applications. *J. Power Sources* **2018**, *396*, 429–436.

[25] Wang, H. K.; Qian, R. F.; Cheng, Y. H.; Wu, H. H.; Wu, X. W.; Pan, K. M.; Zhang, Q. B. Micro/nanostructured $TiNb_2O_7$-related electrode materials for high-performance electrochemical energy storage: Recent advances and future prospects. *J. Mater. Chem. A* **2020**, *8*, 18425–18463.

[26] Yuan, T.; Luo, S. N.; Soule, L.; Wang, J. H.; Wang, Y. C.; Sun, D. W.; Zhao, B. T.; Li, W. W.; Yang, J. H.; Zheng, S. Y. et al. A hierarchical $Ti_2Nb_{10}O_{29}$ composite electrode for high-power lithium-ion batteries and capacitors. *Mater. Today* **2021**, *45*, 8–19.

[27] Deng, S. J.; Zhu, H.; Wang, G. Z.; Luo, M.; Shen, S. H.; Ai, C. Z.; Yang, L.; Lin, S. W.; Zhang, Q. H.; Gu, L. et al. Boosting fast energy storage by synergistic engineering of carbon and deficiency. *Nat. Commun.* **2020**, *11*, 132.

[28] Zhao, L. J.; Wang, S. T.; Dong, Y. H.; Quan, W.; Han, F.; Huang, Y. M.; Li, Y. T.; Liu, X. H.; Li, M. D.; Zhang, Z. T. et al. Coarse-grained reduced $Mo_xTi_{1-x}Nb_2O_{7+y}$ anodes for high-rate lithium-ion batteries. *Energy Stor. Mater.* **2021**, *34*, 574–581.

[29] He, Y. H.; Matthews, B.; Wang, J. Y.; Song, L.; Wang, X. X.; Wu, G. Innovation and challenges in materials design for flexible rechargeable batteries: From 1D to 3D. *J. Mater. Chem. A* **2018**, *6*, 735–753.

[30] An, Y. L.; Tian, Y.; Wei, C. L.; Tao, Y.; Xi, B. J.; Xiong, S. L.; Feng, J. K.; Qian, Y. T. Dealloying: An effective method for scalable fabrication of 0D, 1D, 2D, 3D materials and its application in energy storage. *Nano Today* **2021**, *37*, 101094.

[31] Yang, C.; Yu, S.; Lin, C. F.; Lv, F.; Wu, S. Q.; Yang, Y.; Wang, W.; Zhu, Z. Z.; Li, J. B.; Wang, N. et al. $Cr_{0.5}Nb_{24.5}O_{62}$ nanowires with high electronic conductivity for high-rate and long-life lithium-ion storage. *ACS Nano* **2017**, *11*, 4217–4224.

[32] Park, H.; Song, T.; Paik, U. Porous $TiNb_2O_7$ nanofibers decorated with conductive $Ti_{1-x}Nb_xN$ bumps as a high power anode material for Li-ion batteries. *J. Mater. Chem. A* **2015**, *3*, 8590–8596.

[33] Cheng, X. L.; Sun, Y. J.; Li, D. J.; Yang, H.; Chen, F.; Huang, F. Y.; Jiang, Y.; Wu, Y.; An, X. T.; Yu, Y. From 0D to 3D: Dimensional control of bismuth for potassium storage with superb kinetics and cycling stability. *Adv. Energy Mater.* **2021**, *11*, 2102263.

[34] Guo, B. K.; Yu, X. Q.; Sun, X. G.; Chi, M. F.; Qiao, Z. A.; Liu, J.; Hu, Y. S.; Yang, X. Q.; Goodenough, J. B.; Dai, S. A long-life lithium-ion battery with a highly porous $TiNb_2O_7$ anode for large-scale electrical energy storage. *Energy Environ. Sci.* **2014**, *7*, 2220–2226.

[35] Zhu, R. M.; Duan, H. Y.; Zhao, Z. M.; Pang, H. Recent progress of dimensionally designed electrode nanomaterials in aqueous electrochemical energy storage. *J. Mater. Chem. A* **2021**, *9*, 9535–9572.

[36] Cheng, Q. S.; Liang, J. W.; Lin, N.; Guo, C.; Zhu, Y. C.; Qian, Y. T. Porous $TiNb_2O_7$ nanospheres as Ultra long-life and high-power anodes for lithium-ion batteries. *Electrochim. Acta* **2015**, *176*, 456–462.

[37] Niederberger, M.; Pinna, N. *Metal Oxide Nanoparticles in Organic Solvents: Synthesis, Formation, Assembly and Application*. Springer Science & Business Media: London, 2009.

[38] Pinna, N.; Niederberger, M. Surfactant-free nonaqueous synthesis of metal oxide nanostructures. *Angew. Chem. Int. Ed.* **2008**, *47*, 5292–5304.

[39] Skrodczky, K.; Antunes, M. M.; Han, X. Y.; Santangelo, S.; Scholz, G.; Valente, A. A.; Pinna, N.; Russo, P. A. Niobium pentoxide nanomaterials with distorted structures as efficient acid catalysts. *Commun. Chem.* **2019**, *2*, 129.

[40] Deshmukh, R.; Niederberger, M. Mechanistic aspects in the formation, growth and surface functionalization of metal oxide nanoparticles in organic solvents. *Chem. Eur. J* **2017**, *23*, 8542–8570.

[41] Niederberger, M.; Garnweitner, G. Nonaqueous synthesis of barium titanate nanocrystals in acetophenone as oxygen supplying agent. *MRS Online Proc. Library* **2005**, *879*, 98.

[42] Han, X. Y.; Wahl, S.; Russo, P. A.; Pinna, N. Cobalt-assisted morphology and assembly control of Co-doped ZnO nanoparticles. *Nanomaterials* **2018**, *8*, 249.

[43] Li, W. H.; Zamani, R.; Ibáñez, M.; Cadavid, D.; Shavel, A.; Morante, J. R.; Arbiol, J.; Cabot, A. Metal ions to control the morphology of semiconductor nanoparticles: Copper selenide nanocubes. *J. Am. Chem. Soc.* **2013**, *135*, 4664–4667.

[44] Selishcheva, E.; Parisi, J.; Kolny-Olesiak, J. Copper-assisted shape control in colloidal synthesis of indium oxide nanoparticles. *J. Nanopart. Res.* **2012**, *14*, 711.

[45] Zhu, X. Z.; Fu, Q. F.; Tang, L. F.; Lin, C. F.; Xu, J.; Liang, G. S.; Li, R. J.; Luo, L. J.; Chen, Y. J. $Mg_2Nb_{34}O_{87}$ porous microspheres for use in high-energy, safe, fast-charging, and stable lithium-ion batteries. *ACS Appl. Mater. Interfaces* **2018**, *10*, 23711–23720.

[46] Shen, S. H.; Zhang, S. Z.; Deng, S. J.; Pan, G. X.; Wang, Y. D.; Liu, Q.; Wang, X. L.; Xia, X. H.; Tu, J. P. Bioinspired large-scale production of multidimensional high-rate anodes for both liquid &

solid-state lithium ion batteries. *J. Mater. Chem. A* **2019**, *7*, 22958–22966.
[47] Wadsley, A. D. Mixed oxides of titanium and niobium. *I. Acta Crystallogr.* **1961**, *14*, 660–664.
[48] Liu, A.; Zhang, H. T.; Xing, C. X.; Wang, Y. L.; Zhang, J. W.; Zhang, X. X.; Zhang, S. J. Intensified energy storage in high-voltage nanohybrid supercapacitors via the efficient coupling between $TiNb_2O_7$/holey-rGO nanoarchitectures and ionic liquid-based electrolytes. *ACS Appl. Mater. Interfaces* **2021**, *13*, 21349–21361.
[49] Meng, J. S.; He, Q.; Xu, L. H.; Zhang, X. C.; Liu, F.; Wang, X. P.; Li, Q.; Xu, X. M.; Zhang, G. B.; Niu, C. J. et al. Identification of phase control of carbon-confined Nb_2O_5 nanoparticles toward high-performance lithium storage. *Adv. Energy Mater.* **2019**, *9*, 1802695.
[50] Baek, S. W.; Wyckoff, K. E.; Butts, D. M.; Bienz, J.; Likitchatchawankun, A.; Preefer, M. B.; Frajnkovič, M.; Dunn, B. S.; Seshadri, R.; Pilon, L. *Operando* calorimetry informs the origin of rapid rate performance in microwave-prepared $TiNb_2O_7$ electrodes. *J. Power Sources* **2021**, *490*, 229537
[51] Liu, M. N.; Yan, C.; Zhang, Y. G. Fabrication of Nb_2O_5 nanosheets for high-rate lithium ion storage applications. *Sci. Rep.* **2015**, *5*, 8326.
[52] Uceda, M.; Chiu, H. C.; Zhou, J. G.; Gauvin, R.; Zaghib, K.; Demopoulos, G. P. Nanoscale assembling of graphene oxide with electrophoretic deposition leads to superior percolation network in Li-ion electrodes: $TiNb_2O_7$/rGO composite anodes. *Nanoscale* **2020**, *12*, 23092–23104.
[53] Lin, C. F.; Deng, S. J.; Kautz, D. J.; Xu, Z. H.; Liu, T.; Li, J. B.; Wang, N.; Lin, F. Intercalating $Ti_2Nb_{14}O_{39}$ anode materials for fast-charging, high-capacity and safe lithium-ion batteries. *Small* **2017**, *13*, 1702903.
[54] Feng, T. Y.; Xu, Y. L.; Zhang, Z. W.; Du, X. F.; Sun, X. F.; Xiong, L. L.; Rodriguez, R.; Holze, R. Low-cost Al_2O_3 coating layer as a preformed SEI on natural graphite powder to improve coulombic efficiency and high-rate cycling stability of lithium-ion batteries. *ACS Appl. Mater. Interfaces* **2016**, *8*, 6512–6519.
[55] Ren, J. G.; Wu, Q. H.; Hong, G.; Zhang, W. J.; Wu, H. M.; Amine, K.; Yang, J. B.; Lee, S. T. Silicon-graphene composite anodes for high-energy lithium batteries. *Energy Technol.* **2013**, *1*, 77–84.
[56] Huang, S. Z.; Zhang, L.; Liu, L. F.; Liu, L. X.; Li, J. J.; Hu, H.; Wang, J. W.; Ding, F.; Schmidt, O. G. Rationally engineered amorphous TiO_x/Si/TiO_x nanomembrane as an anode material for high energy lithium ion battery. *Energy Stor. Mater.* **2018**, *12*, 23–29.
[57] Domi, Y.; Usui, H.; Iwanari, D.; Sakaguchi, H. Effect of mechanical pre-lithiation on electrochemical performance of silicon negative electrode for lithium-ion batteries. *J. Electrochem. Soc.* **2017**, *164*, A1651–A1654.
[58] Xu, H.; Li, S.; Zhang, C.; Chen, X. L.; Liu, W. J.; Zheng, Y. H.; Xie, Y.; Huang, Y. H.; Li, J. Roll-to-roll prelithiation of Sn foil anode suppresses gassing and enables stable full-cell cycling of lithium ion batteries. *Energy Environ. Sci.* **2019**, *12*, 2991–3000.
[59] Yang, L. T.; Zhu, X. Z.; Li, X. H.; Zhao, X. B.; Pei, K.; You, W. B.; Li, X.; Chen, Y. J.; Lin, C. F.; Che, R. C. Conductive copper niobate: Superior Li^+-storage capability and novel Li^+-transport mechanism. *Adv. Energy Mater.* **2019**, *9*, 1902174.
[60] Hong, Z. S.; Zhen, Y. C.; Ruan, Y. R.; Kang, M. L.; Zhou, K. Q.; Zhang, J. M.; Huang, Z. G.; Wei, M. D. Rational design and general synthesis of S-doped hard carbon with tunable doping sites toward excellent Na-ion storage performance. *Adv. Mater.* **2018**, *30*, 1802035.
[61] Griffith, K. J.; Wiaderek, K. M.; Cibin, G.; Marbella, L. E.; Grey, C. P. Niobium tungsten oxides for high-rate lithium-ion energy storage. *Nature* **2018**, *559*, 556–563.
[62] Griffith, K. J.; Senyshyn, A.; Grey, C. P. Structural stability from crystallographic shear in TiO_2-Nb_2O_5 Phases: Cation ordering and lithiation behavior of $TiNb_{24}O_{62}$. *Inorg. Chem.* **2017**, *56*, 4002–4010.
[63] Ise, K.; Morimoto, S.; Harada, Y.; Takami, N. Large lithium storage in highly crystalline $TiNb_2O_7$ nanoparticles synthesized by a hydrothermal method as anodes for lithium-ion batteries. *Solid State Ion.* **2018**, *320*, 7–15.
[64] Yan, L.; Shu, J.; Li, C. X.; Cheng, X.; Zhu, H. J.; Yu, H. X.; Zhang, C. F.; Zheng, Y.; Xie, Y.; Guo, Z. P. $W_3Nb_{14}O_{44}$ nanowires: Ultrastable lithium storage anode materials for advanced rechargeable batteries. *Energy Stor. Mater.* **2019**, *16*, 535–544
[65] Xu, W. L.; Russo, P. A.; Schultz, T.; Koch, N.; Pinna, N. Niobium-doped titanium dioxide with high dopant contents for enhanced lithium-ion storage. *ChemElectroChem* **2020**, *7*, 4016–4023.
[66] Wang, D. L.; Yu, Y. C.; He, H.; Wang, J.; Zhou, W. D.; Abruña, H. D. Template-free synthesis of hollow-structured Co_3O_4 nanoparticles as high-performance anodes for lithium-ion batteries. *ACS Nano* **2015**, *9*, 1775–1781.
[67] Wang, J. C.; Gao, G. H.; Zhou, X. W.; Wu, J. D.; Yang, H. Y.; Li, Q.; Wu, G. M. A facile method to prepare bi-phase lithium vanadate as cathode materials for Li-ion batteries. *J. Solid State Electrochem.* **2014**, *18*, 2459–2467.
[68] Augustyn, V.; Come, J.; Lowe, M. A.; Kim, J. W.; Taberna, P. L.; Tolbert, S. H.; Abruña, H. D.; Simon, P.; Dunn, B. High-rate electrochemical energy storage through Li^+ intercalation pseudocapacitance. *Nat. Mater.* **2013**, *12*, 518–522.
[69] Simon, P.; Gogotsi, Y.; Dunn, B. Where do batteries end and supercapacitors begin. *Science* **2014**, *343*, 1210–1211.
[70] Brezesinski, T.; Wang, J.; Tolbert, S. H.; Dunn, B. Ordered mesoporous α-MoO_3 with iso-oriented nanocrystalline walls for thin-film pseudocapacitors. *Nat. Mater.* **2010**, *9*, 146–151.
[71] Singh, M.; Kaiser, J.; Hahn, H. Thick electrodes for high energy lithium ion batteries. *J. Electrochem. Soc.* **2015**, *162*, A1196–A1201.
[72] Catti, M.; Pinus, I.; Knight, K. Lithium insertion properties of $Li_xTiNb_2O_7$ investigated by neutron diffraction and first-principles modelling. *J. Solid State Chem.* **2015**, *229*, 19–25.
[73] AbdelHamid, A. A.; Mendoza-Garcia, A.; Ying, J. Y. Advances in and prospects of nanomaterials' morphological control for lithium rechargeable batteries. *Nano Energy* **2022**, *93*, 106860.
[74] Cong, L. N.; Xie, H. M.; Li, J. H. Hierarchical structures based on two-dimensional nanomaterials for rechargeable lithium batteries. *Adv. Energy Mater.* **2017**, *7*, 1601906.
[75] Jumas, J. C.; Sougrati, M. T.; Perea, A.; Aldon, L.; Olivier-Fourcade, J. Combined *operando* studies of new electrode materials for Li-ion batteries. *Hyperfine Interact.* **2013**, *217*, 107–115.
[76] Petříček, V.; Dušek, M.; Palatinus, L. Crystallographic computing system JANA2006: General features. *Z. Kristallogr. Cryst. Mater.* **2014**, *229*, 345–352.